

Measurements and simulation of ionospheric scattering on VHF and UHF radar signals: Channel scattering function

Neil C. Rogers,¹ Paul S. Cannon,¹ and Keith M. Groves²

Received 8 October 2008; revised 3 February 2009; accepted 4 March 2009; published 9 June 2009.

[1] The design and operation of transionospheric VHF and UHF radars requires knowledge of amplitude and phase scintillation due to ionospheric scattering. Phase coherence is of particular importance where long coherent integration periods and large bandwidths are required. A thin phase screen, parabolic equation based, Trans-Ionospheric Radio Propagation Simulator (TIRPS) is described. Modeled channel scattering functions (CSFs) are compared to experimental VHF and UHF data derived from the Advanced Research Projects Agency Long-range Tracking and Instrumentation Radar on Kwajalein Island (9.4°N, 166.8°E). TIRPS quantitatively reproduces the experimental results, including the quasi-parabolic profile observed in the measured CSFs under strong turbulence conditions. Variations in the simulated CSF with ionospheric phase screen parameters are also presented. Under conditions of high integrated strength of turbulence (C_kL), a low phase spectral index ($p = 1$), indicating relatively dense small-scale irregularities, produces pronounced range spreading. Conversely, when the spectral index is high ($p = 4$), indicative of strong focusing/defocusing by large-scale irregularities, there is increased Doppler spreading and, when the outer scale of irregularities is large, a greater likelihood of asymmetry of the CSF about the zero Doppler axis.

Citation: Rogers, N. C., P. S. Cannon, and K. M. Groves (2009), Measurements and simulation of ionospheric scattering on VHF and UHF radar signals: Channel scattering function, *Radio Sci.*, 44, RS0A07, doi:10.1029/2008RS004033.

1. Introduction

[2] In recent years the feasibility of space-based synthetic aperture radar (SAR) operating at frequencies below 500 MHz has been examined for both environmental monitoring [Rignot *et al.*, 1995] and military applications when foliage- and ground-penetrating properties are required. Radars operating between 420 and 450 MHz are also used for ground-based radar space-object tracking.

[3] Unfortunately, at these low frequencies, the ionosphere can cause significant pulse distortion [Belcher, 2008], polarization rotation [Wright *et al.*, 2003] and loss of phase coherence across a synthesized aperture [van de Kamp *et al.*, 2009] and over a pulse integration period. This is particularly true in the equatorial region ($\pm 20^\circ$ geomagnetic latitude) where the ionosphere can be highly structured and turbulent, forming irregularities in the electron density. These irregularities scatter the

radio signals, causing amplitude and phase fluctuations known as scintillation.

[4] Understanding and mitigating these effects is critical in the design of transionospheric radar systems, particularly wideband systems. The effects of two-way (backscattered) propagation through a strongly turbulent atmosphere was first investigated by Yeh [1983], who derived expressions for the backscattered intensity and the mutual coherence between forward and backscattered waves. Knepp and Houppis [1991] extended this theory and experimentally demonstrated the predicted enhancements in backscattered signal intensity for a monostatic radar. More recently, Cannon *et al.* [2006] presented the ionospheric distortion on wideband transionospheric VHF and UHF radar waveforms in terms of the channel scattering function (CSF) [Bello, 1963]. The CSF is a representation of the time-varying complex impulse response of a backscattered radar waveform which provides a simultaneous characterization of both ionospheric induced delay spread and Doppler spread.

[5] In this paper we describe a model of the transionospheric distortion and we compare it to sample channel scattering measurements. In a companion paper (N. C. Rogers *et al.*, Measurements and simulation of ionospheric scattering on VHF and UHF radar signals:

¹RF Operational Environments, QinetiQ, Malvern, UK.

²Air Force Research Laboratory, Hanscom Air Force Base, Massachusetts, USA.

Coherence times, coherence bandwidths, and S_4 , submitted to *Radio Science*, 2008) we extend this analysis to a larger data set to quantify important parameters such as coherency time and coherence bandwidth.

2. Measurements of the Transionospheric Channel Scattering Function

[6] Our measurements were conducted as part of the joint UK/U.S. Wideband Ionospheric Distortion Experiment (WIDE) which employed the Advanced Research Projects Agency Long-range Tracking and Instrumentation Radar (ALTAIR). This is a monostatic radar located at the Ronald Reagan Ballistic Missile Defense Test Site (RTS) on Kwajalein Atoll (9.395 °N, 167.469 °E). It employs a 6 MW transmitter which feeds a 42-m-diameter parabolic dish. Upgoing linear frequency-modulated radar chirps were transmitted simultaneously at 158 MHz (7 MHz bandwidth) and 422 MHz (18 MHz bandwidth) with a pulse repetition frequency (PRF) in the range 285 ± 50 Hz with PRF changes occurring no more than once every 20 s.

[7] The results presented here describe signals transmitted to, and reflected back from, a calibration sphere (object 2826 in the NORAD catalog) of 0.3 m^2 radar cross section (optical) in an orbit at 767 ± 6 km altitude and at 70° inclination. The sphere presented a constant aspect angle insensitive radar cross section, ensuring that any scintillation observed was due to atmospheric signal distortion rather than target tumbling. A 20° elevation mask was used to exclude measurements that might be contaminated by ground multipath. The radar measured a combination of the Doppler frequency shift due to target's range rate and a shift and spread in the Doppler frequency imposed by the irregular ionospheric medium. The Doppler frequency component due to target range rate has been subtracted from the radar measurements, as has the component due to bulk ionospheric refraction (as calculated from the relative delay of 158 and 422 MHz signals).

[8] The impact of the ionosphere on wideband radio signals has been represented by a channel scattering function (CSF), which is a measure of the channel's time-varying complex impulse response and maps the signal power distribution in group delay and Doppler frequency. The CSF was calculated from sequences of 1024 contiguous radar chirp returns which, at an average pulse repetition frequency (PRF) of 285 Hz, constitute a 3.6 s sample. Each returned chirp was pulse-compressed (cross-correlated with a replica of the transmitted chirp) using a Hann filter, and the component of pulse spreading due to ionospheric dispersion was removed by calculating the total electron content (TEC) from the differential group delay of the 158 and 422 MHz chirp returns. The horizontal scale of the CSF represents the delay of the

pulse-compressed chirp. For each delay sample (or range gate), the sequence of 1024 pulse-compressed chirps was transformed into a Doppler spectrum using a Fast Fourier Transform (FFT). Thus the temporal variation of the CIR in each range gate (or delay sample) over the 3.6 s period is represented as a Doppler spectrum (the vertical scale on the CSF).

[9] Examples of the CSF for the 158 MHz and 422 MHz chirps are presented in Figure 1 for four CSFs recorded on the 18 January 2005 pass. Figure 1a is an example of low Doppler spread and minimal delay spreading (limited by the system sampling rate); note the greater noise level in the 158 MHz CSF (Figure 1, left). Figure 1b exhibits moderate Doppler spreading. In contrast, in Figures 1c and 1d the Doppler spreading is considerable (tens of Hz), indicating rapid pulse-to-pulse fading. The 158 MHz CSFs in Figures 1c and 1d also exhibit strong delay spreading, where the energy is spread into quasi-parabolic "horns," increasing in Doppler frequency offset with increasing relative delay.

3. Simulations of Channel Scattering Functions

[10] In order to better understand these measurements, the Trans-Ionospheric Radar Propagation Simulator (TIRPS) has been developed to simulate the effects of ionospheric scintillation on wideband waveforms. The model uses a split-step parabolic equation (PE) technique [Levy, 2000; Knepp, 1983] to provide a good approximation to the full electromagnetic wave equation under the paraxial approximation (i.e., where the signal is forward scattered over narrow angles of deflection about the axis of propagation). The ionosphere is represented by a one-dimensional thin phase screen at an altitude of 350 km (the approximate height of the F layer maximum). The phase screen is aligned in the direction of minimum ionospheric spatial coherence (i.e., aligned east-west across the geomagnetic field lines, assuming the irregularities are field-aligned). Following Knepp [1983], the phase screen $\phi(x, f_0)$ appropriate for a radio wave component at the carrier frequency f_0 , is generated by filtering a normally distributed, zero-mean random sequence by the analytical spatial spectrum proposed by Rino [1979] (equation (1)).

$$S_\phi(\kappa) = \left[\frac{1}{4} \pi^{-\frac{3}{2}} r_e^2 \left(\frac{c}{f_0} \right)^2 G C_k L \sec(\theta) \left(\frac{2\pi}{1000} \right)^{p+1} \frac{\Gamma(\frac{p}{2})}{\Gamma(\frac{p+1}{2})} \right] \cdot \frac{1}{(\kappa_0^2 + \kappa^2)^{p/2}} \quad (1)$$

where

κ spatial frequency;

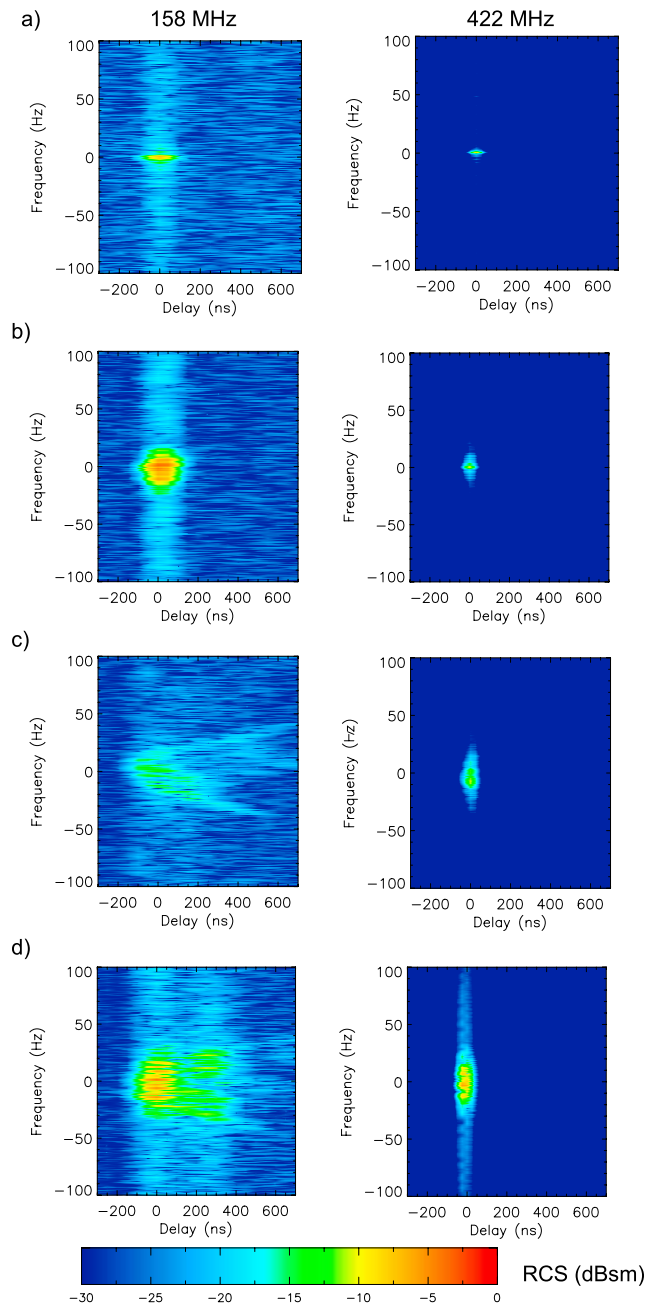


Figure 1. Examples of ALTAIR CSF measured during the 18 January 2005 pass of satellite 2826 at (left) 158 MHz and (right) 422 MHz. (a) Low Doppler spread and minimal delay spreading (limited by the system sampling rate). (b) Moderate Doppler spreading. (c and d) Considerable Doppler spreading (tens of Hz).

- r_e classical electron radius;
 c speed of radio wave propagation in free space;
 f_0 carrier frequency (chirp center frequency);
 G geometric enhancement factor [see *Rino*, 1979, 1982];
 $C_k L$ vertical integrated strength of turbulence at the 1 km scale;
 θ propagation zenith angle at ionospheric pierce point;
 p phase spectral index;
 $\Gamma()$ Euler's gamma function;
 κ_o outer-scale frequency equal to $2\pi/L_o$.

[11] This idealized spectrum provides a smooth transition from a flat spectrum at scales greater than L_o (the outer-scale size for turbulence) and a log-log linear spectrum (typical of turbulent energy-cascading processes) with the form $S_\phi(\kappa) \propto \kappa^{-p}$ for scales below L_o . The simulator produces a single random realization of the phase screen whose spatial spectrum approximates to the ideal spectrum of equation (1). The average spectrum of an increasing number of realizations would converge to the ideal spectrum.

[12] Under the paraxial approximation it is convenient to define a “reduced” complex field u such that the electric field component of the radio wave is given as

$$E(x, z, f) \equiv u(x, z, f) \exp\left(i \frac{2\pi c}{f} z\right) \quad (2)$$

where f is the radio frequency, thus removing the oscillatory component of the field along the axis of propagation, z . If the reduced field incident on the phase screen at $z = 0$ is $u(x, 0, f)$, then the field emerging from the phase screen is simply phase-advanced by the phase in the phase screen, i.e.,

$$\begin{aligned} u(x, 0_+, f) &= u(x, 0, f) \exp(i\phi(x, f)) \\ &= u(x, 0, f) \exp\left(i \frac{f_0}{f} \phi(x, f_0)\right) \end{aligned} \quad (3)$$

noting that the phase screen's phase is proportional to $1/f$. The second step in this split-step PE technique is to calculate the development of the emergent wave after it has propagated a distance z through free space. The technique, which is analogous to Fresnel-Kirchhoff diffraction, requires the multiplication of the wave's spatial spectrum by the “free space propagator” $\exp\left(i \frac{c}{4\pi f} \kappa^2 z\right)$, thus:

$$u(x, z, f) = F^{-1} \left\{ F[u(x, 0_+, f)] \exp\left(i \frac{c}{4\pi f} \kappa^2 z\right) \right\} \quad (4)$$

where $F[u(x, \dots)] = U(\kappa, \dots)$ and $F^{-1}[U(\kappa, \dots)] = u(x, \dots)$ represent a Fourier transform pair.

[13] The PE method above is used to determine the complex signal spectrum of an unmodulated planar wave propagated one-way through the phase screen. Since the wave incident on the phase screen is spherically divergent, rather than planar, a “reduced” propagation distance [Rino, 1982] from the phase screen z_R is used:

$$z_R = \frac{z_1 z_2}{z_1 + z_2} \quad (5)$$

where z_1 is the range from radar to the phase screen and z_2 is the range from phase screen to the target. The use of the planar phase screen theory with this correction is a satisfactory approximation except where $z_1/(z_1 + z_2) \ll 1$ or $z_2/(z_1 + z_2) \ll 1$ [see, e.g., Lee, 1977].

[14] The signal of the chirp-modulated wave is obtained by filtering the unmodulated field u with the spectrum of the transmitted waveform. The baseband spectrum of the upgoing linear frequency-modulated chirps transmitted by ALTAIR may be expressed as [Klauder et al., 1960]:

$$M(f_d) = \sqrt{\frac{T_{ch}}{2\Delta}} \exp\left(-i \frac{\pi T_{ch} f_d^2}{\Delta}\right) [Z(b_+) - Z(b_-)] \quad (6)$$

where Δ is the frequency sweep range (or “chirp bandwidth”), T_{ch} is the chirp duration, and f_d is the $f - f_0$ (the Doppler frequency).

$$b_+ = -2f_d \sqrt{\frac{T_{ch}}{2\Delta}} + \sqrt{\frac{T_{ch}\Delta}{2}} \quad (7)$$

$$b_- = -2f_d \sqrt{\frac{T_{ch}}{2\Delta}} - \sqrt{\frac{T_{ch}\Delta}{2}} \quad (8)$$

and $Z()$ is the complex Fresnel integral given by

$$Z(b) = \int_0^b e^{i\pi a^2/2} da \quad (9)$$

The modulated signal phase and amplitude u_{up} is thus determined at each point in the orbit for which a pulse is reflected by the target. The time separation between upward and downward ionospheric transitions is just 3 ms at zenith or 6 ms at 20° elevation, so given that ionospheric drift speeds are typically around 100 ms⁻¹ in the equatorial region, the ionospheric motion (up to 0.6 m) is well below the inner-scale size for field-aligned irregularities (approximately 2–5 m [Wheelon, 2001, p. 97]) and so is negligible. The received field pattern following two-way transition $u_{2-way}(x, f)$ is, therefore, calculated as the square of that on a one-way path $u_{up}(x, f)$, noting that z_R is the same on up and down paths.

[15] The pulse-compressed complex impulse response (CIR) is then determined for each transverse position x :

$$\begin{aligned} CIR(x, \tau) &= \mathbf{F}^{-1} [M(f_d)H(f_d)u_{2-way}(x, f)M(f, d)^*H(f, d)^*] \end{aligned} \quad (10)$$

where $H(f_d) = \mathbf{F}[h(\tau)]$ is the temporal FFT of the Hann function which is used to pulse shape the waveform and its matched filter. A spatial FFT from x to κ (using a Hann filter $h(x)$) is then used to produce a spatial CSF

$$CSF(\kappa, \tau) = \mathbf{F}[CIR(x, \tau)h(x)] \quad (11)$$

The satellite velocity vector does not generally align with the phase screen which is perpendicular to the principal axis of the irregularities. Therefore, to convert from a spatial to a temporal CSF (for comparison with those recorded by ALTAIR) the model uses an effective scan velocity v_{eff} of the ionospheric pierce point (IPP) along the phase screen [Rino, 1982]. This is based on the satellite and ionospheric drift velocities; the alignment of the irregularities relative to both the geomagnetic field and the radio propagation vector; and the axial ratios of the irregularities. Details of its calculation are given in Appendix A. Given that the diffraction pattern at orbital height is sampled at the radar PRF, the required spatial sampling interval is

$$dx = \frac{v_{eff}}{PRF} \left(\frac{z_1 + z_2}{z_1} \right) \quad (12)$$

where the factor $(z_1 + z_2)/z_1$ corrects for the spherical divergence between phase screen and target range.

[16] Ionospheric drift velocity forms a small component of the IPP scan velocity. In the following simulations we have assumed an approximate ionospheric drift velocity of 100 ms^{-1} in the geomagnetic east direction. While no drift measurements were available for 18 January 2005, this approximation is based on typical drift velocities measured at similar local times using a correlation analysis of VHF geosynchronous satellite beacon signals received on east-west spaced antennas on Kwajalein atoll (part of the global monitoring network for SCINDA (Scintillation Network Decision Aid)). An axial ratio of 30:1:1 has been assumed for irregularities aligned to a geomagnetic field determined by the U.S./UK World Magnetic Model [McLean et al., 2004].

[17] To help prevent aliasing, absorbing layers (half Hann windows) are applied at the extreme eighths of the screen (equation (13)).

$$\begin{aligned} A(x) &= \frac{1}{2} \left(1 + \cos \left[\pi \frac{(x - \frac{1}{8}L_x)}{\frac{1}{8}L_x} \right] \right) , & x < \frac{1}{8}L_x \\ &= 1 , & \frac{1}{8}L_x \leq x \leq \frac{7}{8}L_x \\ &= \frac{1}{2} \left(1 + \cos \left[\pi \frac{(x - \frac{7}{8}L_x)}{\frac{1}{8}L_x} \right] \right) , & x > \frac{7}{8}L_x \end{aligned} \quad (13)$$

where L_x is the length of the screen.

4. Results

[18] In the simulations described below, a phase screen of $N_x = 8192$ points has been implemented. The 40- μs duration 158 MHz chirp waveform was sampled with 1024 points at the ALTAIR radar sampling interval of 50 ns, while the 150 μs 422 MHz chirp was sampled with 8192 points at the radar sampling interval of 25 ns.

[19] Using an effective velocity v_{eff} of 1514 ms^{-1} an elevation of 24° and PRF = 262 Hz (chosen for direct comparison with observations presented in Figures 1c and 1d and assuming a 100 ms^{-1} eastward ionospheric drift), the screen spacing $dx = 11.6 \text{ m}$, giving a total screen length of $N_x dx = 94.8 \text{ km}$. Only the central 1024 points of the field pattern at the target range are used in the calculation of the CSF. For comparison, the first Fresnel zone radius, $\sqrt{z_{RC}/f_0}$ is 857 m at 158 MHz and 524 m at 422 MHz.

[20] The results of the simulations of CSFs, presented below are mainly dependent on three variables used in the phase screen spectrum (equation (1)): p , L_o and C_kL . Empirical climatological models such as WBMOD [Secan et al., 1995] predict C_kL values ranging over several orders of magnitude, peaking at around 10^{36} in the equatorial, postsunset ionosphere. In equation (1), C_kL is augmented by geometric factors G [Rino, 1979] and $\sec(\theta)$ which are both of order 1; so the simulations presented below treat $G C_kL \sec(\theta)$ as a single combined variable. Measurements of phase spectral index, p , reported in the literature generally range between 1 and 4, with a mode between 2.5 and 2.8. [e.g., Livingston et al., 1981]. Outer-scale lengths, L_o , also vary widely over an approximate range of 5 to 20 km [Wheeler, 2001, p. 96].

[21] Results of TIRPS simulations of the CSFs recorded in Figure 1 are presented in Figure 2 for 158 MHz (Figure 2, left) and 422 MHz (Figure 2, right). These have used system and orbit parameters appropriate to the examples in Figures 1c and 1d with midrange

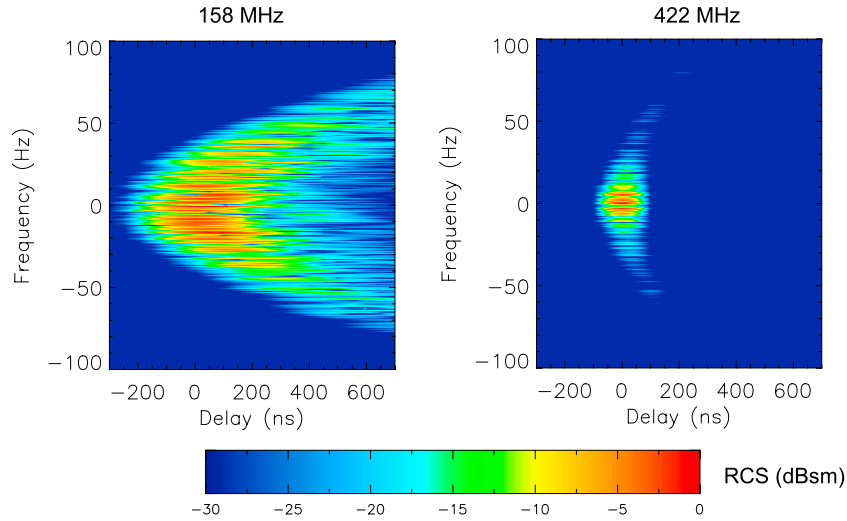


Figure 2. TIRPS simulations of the ALTAIR CSF (normalized to 0 dB m²) for (left) 158 MHz and (right) 422 MHz. PRF = 262 Hz, elevation is equal to 24°, azimuth is equal to 8°, $G C_k L \sec(\theta) = 10^{35}$, $v_{\text{eff}} = 1514 \text{ ms}^{-1}$, $p = 2.5$, and $L_o = 10 \text{ km}$.

values of $p = 2.5$, $L_o = 10 \text{ km}$ and a high value of $G C_k L \sec(\theta) = 10^{35}$. The standard deviation of phase in the phase screen, σ_ϕ , was 12.6 and 4.6 radians for 158 MHz and 422 MHz, respectively. The simulation provides a good reproduction of the main features of the ALTAIR CSFs at both frequencies, including the characteristic quasi-parabolic increases in delay with increasing Doppler offset.

[22] Figure 3 presents the variation of the simulated CSF for the 158 MHz waveform for $C_k L$ increasing over

4 orders of magnitude, while keeping other phase screen parameters unchanged. In these simulations σ_ϕ was 0.5, 1.3, 4.7, 12.6 radians for $G C_k L \sec(\theta) = 32, 33, 34, 35$, respectively. This sequence of CSFs illustrates the increase in Doppler spreading and the spread of energy into the horns with increasing turbulence strength.

[23] Figure 4 presents 158 MHz CSF simulations for which the $C_k L$ is kept constant at 10^{34} while p and L_o are varied through most of their natural range. Evidently the proportion of energy in the horns is greatest when the

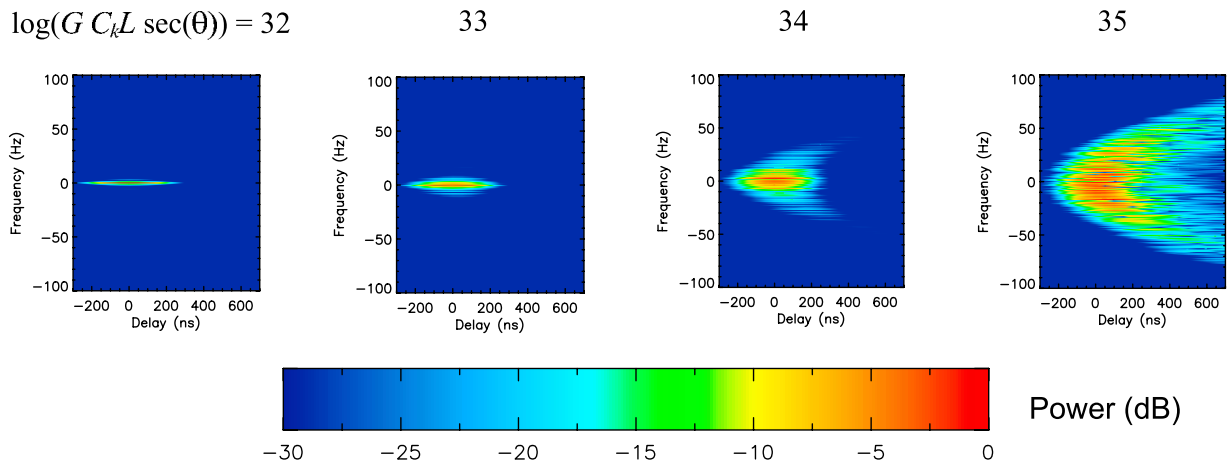


Figure 3. TIRPS simulations of ALTAIR 158 MHz CSF with varying $G C_k L \sec(\theta)$. (Fixed parameters: $p = 2.5$, $L_o = 10 \text{ km}$, PRF = 262 Hz, elevation is equal to 24°, azimuth is equal to 8°, and $v_{\text{eff}} = 1514 \text{ ms}^{-1}$.)

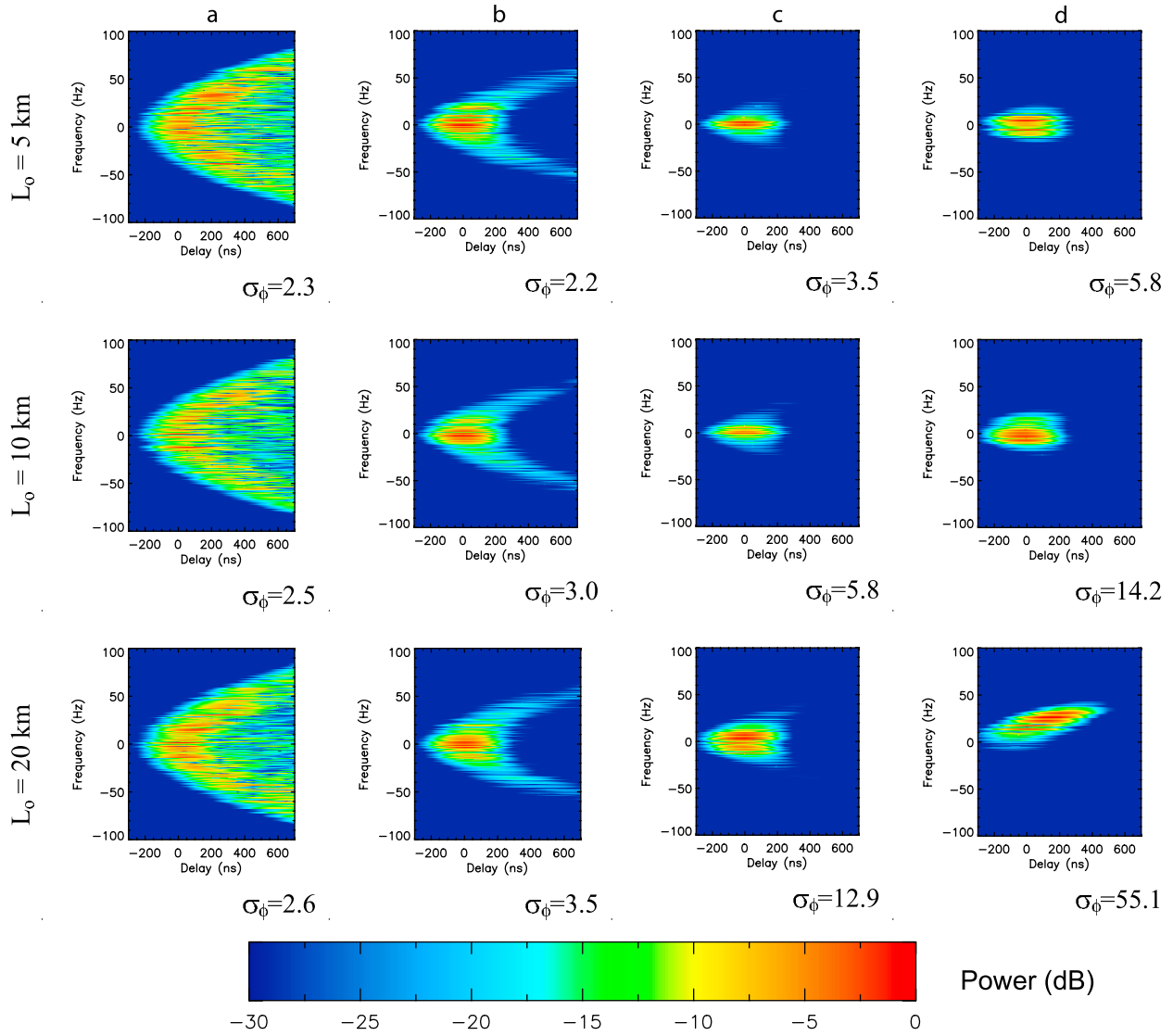


Figure 4. TIRPS simulations of ALTAIR 158 MHz CSF with varying phase screen phase spectral index p and outer-scale L_o . (Fixed parameters: PRF = 262 Hz, elevation is equal to 24° , azimuth is equal to 8° , $GC_k L_{sec}(\theta) = 10^{34}$, and $v_{eff} = 1514 \text{ ms}^{-1}$.) Phase screen phase standard deviations (σ_ϕ) are given in radians.

phase spectral index p is small (see Figure 4a). Under these conditions small-scale irregularities dominate and scatter the wave through large angles and consequently induce large delay values, τ . Scatterers before and after the moving satellite IPP induce positive and negative Doppler shifts, respectively. As p is increased from 3 to 4 (Figure 4d) there is a slight enhancement in Doppler spreading and for larger outer scales a strong asymmetry often develops about the 0 Hz axis. With larger L_o there is an increased likelihood of a large linear component of signal phase being present over the sample period (1024

pulse returns) and this gives rise to the Doppler offsets observed.

[24] The model has also been applied to satellites in higher, lower-velocity orbits. In these cases the Doppler separation of the CSF horns increased, and they spread to more positive delays.

5. Conclusions

[25] Understanding the transionospheric propagation channel is important in the design of high-performance

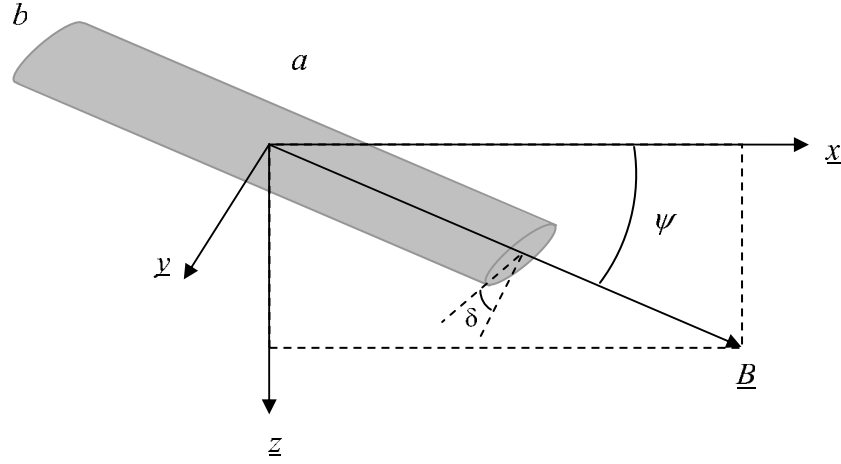


Figure A1. Geometry of an ionospheric irregularity aligned to the geomagnetic field, \underline{B} .

radar systems operating below 1 GHz. Measurements which provide the full complex impulse response (described here through the channel scattering function) are necessarily limited through time and cost, and a robust and validated modeling approach is needed.

[26] By intercomparison between model and measurement we have shown how a thin phase screen, PE technique can indeed simulate the two-way channel scattering functions (CSF) (delay and Doppler power profiles) for an equatorial transionospheric radar. The CSF simulations quantitatively reproduce the delay and Doppler measured using the 158/422 MHz ALTAIR radar and also faithfully reproduce the characteristic features such as the quasi-parabolic “horns.”

[27] The application of the model under extreme conditions of spectral slope also serve to elucidate the reasons why nonuniform scattering is sometimes seen (high spectral index) and why at other times broad spreading of the signal is seen in both Doppler and delay (low spectral index). These results show that with an appropriate choice of phase screen parameters, the TIRPS simulator can be used to assist the design and operation of transionospheric radars performing coherent pulse integration.

Appendix A: Calculation of G and v_{eff}

[28] Ionospheric electron density irregularities are aligned to the geomagnetic field, \underline{B} . Following *Rino* [1982], we describe the shape of an irregularity as the ratio of coherence lengths along and across the field. An illustration of an irregularity of axial ratio $a:b:1$ is shown in Figure A1. Here \underline{x} represents geomagnetic north, \underline{y} is geomagnetic east and \underline{z} is down. Hence \underline{B} lies in the plane $\underline{y} = 0$ and ψ represents the geomagnetic dip (angle from horizontal). a is the largest ratio of coherence length

along the geomagnetic field to that perpendicular to it, while b relates to a secondary axis of elongation perpendicular to a and rotated an angle δ from the \underline{y} axis. Normally $\delta \approx 0$, implying elongation in the magnetic east-west direction (i.e., along the L shell). In this Cartesian frame, the propagation vector, \underline{k} has polar coordinates defined as

$$\underline{k} \equiv \begin{pmatrix} k_x \\ k_y \\ k_z \end{pmatrix} = |\underline{k}| \begin{pmatrix} \sin(\theta) \cos(\varphi) \\ \sin(\theta) \sin(\varphi) \\ \cos(\theta) \end{pmatrix} \hat{\underline{k}} \quad (\text{A1})$$

as illustrated in Figure A2.

[29] The orientation and elongation of the irregularities is important when modeling the ionospheric medium as a single phase screen. In this case the apparent power spectral density of the irregularities is modified by the geometric enhancement factor G , as defined in equation (A2) to equation (A11) below [from *Rino*, 1982].

$$C_{11} = a^2 \cos(\psi)^2 + \sin(\psi)^2 (b^2 \sin(\delta)^2 + \cos(\delta)^2) \quad (\text{A2})$$

$$C_{22} = b^2 \cos(\delta)^2 + \sin(\delta)^2 \quad (\text{A3})$$

$$C_{33} = a^2 \sin(\psi)^2 + \cos(\psi)^2 (b^2 \sin(\delta)^2 + \cos(\delta)^2) \quad (\text{A4})$$

$$C_{12} = (b^2 - 1) \sin(\psi) \sin(\delta) \cos(\delta) \quad (\text{A5})$$

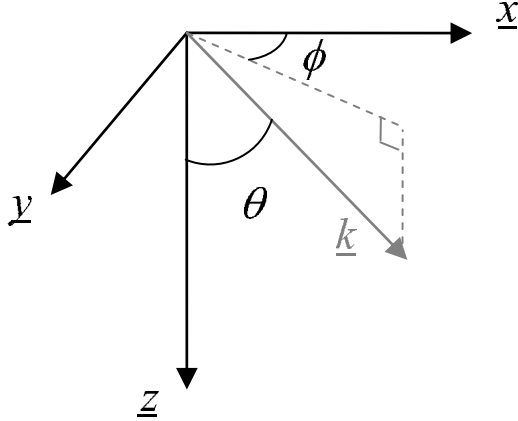


Figure A2. Propagation vector \underline{k} in the local geomagnetic Cartesian reference frame (\underline{x} , \underline{y} , \underline{z}).

$$C_{13} = (a^2 - b^2 \sin^2(\delta) - \cos^2(\delta)) \sin(\psi) \cos(\psi) \quad (\text{A6})$$

$$C_{23} = -(b^2 - 1) \cos(\psi) \sin(\delta) \cos(\delta) \quad (\text{A7})$$

$$A = C_{11} + C_{33} (\tan(\theta)^2 \cos(\phi)^2) - 2C_{13} \tan(\theta) \cos(\phi) \quad (\text{A8})$$

$$B = 2(C_{12} + C_{33} \tan(\theta)^2 \sin(\phi) \cos(\phi) - \tan(\theta)(C_{13} \sin(\phi) + C_{23} \cos(\phi))) \quad (\text{A9})$$

$$C = C_{22} + C_{33} \tan(\theta)^2 \sin(\phi)^2 - 2C_{23} \tan(\theta) \sin(\phi) \quad (\text{A10})$$

$$G = \frac{ab}{\sqrt{AC - \frac{B^2}{4} \cos(\theta)}} \quad (\text{A11})$$

Following *Rino* [1982] and *Secan and Fremouw* [1983], the effective velocity v_{eff} is calculated using the following stages.

[30] 1. Calculate satellite velocity in a Cartesian frame aligned to the transmitted wave propagation direction \underline{k} , up (increasing radar elevation) and right (increasing radar azimuth);

[31] 2. Scale velocity down to that at the ionospheric pierce point (IPP), \underline{v}_{IPP} , by multiplying by the factor $z_1/(z_1 + z_2)$ where z_1 is the range from radar to the IPP and z_2 is the range from IPP to the target. The component of \underline{v}_{IPP} in the direction of propagation \underline{k} is set to zero.

[32] 3. Rotate coordinate frame to determine \underline{v}_{IPP} in geomagnetic coordinates local to the IPP. i.e.,

$$\underline{v}_{IPP} = \begin{pmatrix} v_{IPP,x} \\ v_{IPP,y} \\ v_{IPP,z} \end{pmatrix} \quad (\text{A12})$$

Then, using *Rino's* [1982] derivation of the spatial correlation structure of the phase, we determine the effective velocity as:

$$v_{eff} = \sqrt{\frac{Cv_x^2 - Bv_x v_y + Av_y^2}{AC - \frac{B^2}{4}}} \quad (\text{A13})$$

where

$$v_x = v_{IPP,x} - \tan(\theta) \cos(\phi) v_{IPP,z} \quad (\text{A14})$$

$$v_y = v_{IPP,y} - \tan(\theta) \sin(\phi) v_{IPP,z} \quad (\text{A15})$$

The ionospheric drift velocity, \underline{v}_d , is subtracted from \underline{v}_{IPP} prior to calculation of v_{eff} .

[33] **Acknowledgments.** The UK contribution to this program has been conducted with funding from the United Kingdom Ministry of Defence, Science and Technology program. The MIT Lincoln Laboratory contribution was sponsored by the U.S. Department of the Army under Air Force contract FA8721-05-C-0002. Opinions, interpretations, conclusions, and recommendations are those of the authors and are not necessarily endorsed by the United States government. The authors would like to thank Paul Kossey for his unfailing support in the early stages of this UK-U.S. collaborative program.

References

- Belcher, D. P. (2008), Theoretical limits on SAR imposed by the ionosphere, *IET Radar Sonar Navig.*, 2(6), 435–448, doi:10.1049/iet-rsn:20070188.
- Bello, P. A. (1963), Characterization of randomly time variant linear channels, *IEEE Trans. Commun. Syst.*, CS-11(4), 360–393.
- Cannon, P. S., K. Groves, D. J. Fraser, W. J. Donnelly, and K. Perrier (2006), Signal distortion on VHF/UHF transionospheric paths: First results from the Wideband Ionospheric Distortion Experiment, *Radio Sci.*, 41, RS5S40, doi:10.1029/2005RS003369.
- Klauder, J. R., A. C. Prince, S. Darlington, and W. J. Albersheim (1960), The theory and design of chirp radars, *Bell Syst. Tech. J.*, 39, 745–808.
- Knapp, D. L. (1983), Multiple phase-screen calculation of the temporal behavior of stochastic waves, *Proc. IEEE*, 71(6), 722–737.
- Knapp, D. L., and H. L. F. Houppis (1991), ALTAIR VHF/UHF observations of multipath and backscatter enhancement, *IEEE Trans. Antennas Propag.*, 39(4), 528–534.

- Lee, L. C. (1977), Theory of thin-screen scintillations for a spherical wave, *Astrophys. J.*, 218, 468–476.
- Levy, M. (2000), *Parabolic Equation Methods for Electromagnetic Wave Propagation*, IEE Electromagn. Waves Ser., vol. 45, Inst. of Electr. Eng., London, U. K.
- Livingston, R. C., C. L. Rino, J. P. McClure, and W. B. Hanson (1981), Spectral characteristics of medium-scale equatorial F region irregularities, *J. Geophys. Res.*, 86(A4), 2421–2428.
- McLean, S., S. Macmillan, S. Maus, V. Lesur, A. Thomson, and D. Dater (2004), The US/UK World Magnetic Model for 2005–2010, *Tech. Rep. NESDIS/NGDC-1*, Natl. Oceanic and Atmos. Admin., Boulder, Colo., Dec.
- Rignot, E. J., R. Zimmermann, and J. J. van Zyl (1995), Spaceborne applications of P-band imaging radars for measuring forest biomass, *IEEE Trans. Geosci. Remote Sens.*, 33, 1162–1169.
- Rino, C. L. (1979), A power law phase screen model for ionospheric scintillation: 1. Weak scatter, *Radio Sci.*, 14(6), 1135–1145.
- Rino, C. L. (1982), On the application of phase screen models to the interpretation of ionospheric scintillation data, *Radio Sci.*, 17(4), 855–867.
- Secan, J. A., and E. J. Fremouw (1983), Improvement of the scintillation irregularity model in WBMOD, *Tech. Rep. DNA-TR-81-241*, 95 pp., Def. Nucl. Agency, Washington, D. C., 28 Feb.
- Secan, J. A., R. M. Bussey, E. J. Fremouw, and S. Basu (1995), An improved model of equatorial scintillation, *Radio Sci.*, 30(3), 607–617.
- van de Kamp, M., P. S. Cannon, and M. Terkildsen (2009), Effect of the ionosphere on defocusing of space-based radars, *Radio Sci.*, 44, RS1003, doi:10.1029/2007RS003808.
- Wheelon, A. D. (2001), *Electromagnetic Scintillation, vol. 1, Geometrical Optics*, Cambridge Univ. Press, Cambridge, U. K.
- Wright, P. A., S. Quegan, N. S. Wheadon, and C. D. Hall (2003), Faraday rotation effects on L-band spaceborne SAR data, *IEEE Trans. Geosci. Remote Sens.*, 41(12), 2735–2744.
- Yeh, K. C. (1983), Mutual coherence functions and intensities of backscattered signals in a turbulent medium, *Radio Sci.*, 18(2), 159–165.
-
- P. S. Cannon and N. C. Rogers, RF Operational Environments, QinetiQ, Malvern Technology Centre, St. Andrews Road, Malvern WR14 3PS, UK. (ncrogers@qinetiq.com)
- K. M. Groves, Air Force Research Laboratory, Hanscom Air Force Base, MA 01731, USA.